Conditions for the genesis of early afterdepolarization in a model of a ventricular myocyte *⊗*

Zhikun Chu; Dongping Yang ; Xiaodong Huang



Chaos 30, 043105 (2020)

https://doi.org/10.1063/1.5133086





CrossMark

Articles You May Be Interested In

A model of cardiac ryanodine receptor gating predicts experimental Ca²⁺-dynamics and Ca²⁺-triggered arrhythmia in the long QT syndrome

Chaos (September 2017)

Dynamical analysis of early afterdepolarization patterns in a biophysically detailed cardiac model *Chaos* (July 2021)

Slow [Na⁺]_i dynamics impacts arrhythmogenesis and spiral wave reentry in cardiac myocyte ionic model *Chaos* (August 2017)



Chaos

Special Topic: Nonlinear Model Reduction From Equations and Data

Submit Today!



Conditions for the genesis of early afterdepolarization in a model of a ventricular myocyte

Cite as: Chaos 30, 043105 (2020); doi: 10.1063/1.5133086 Submitted: 23 October 2019 · Accepted: 17 March 2020 · Published Online: 2 April 2020







Zhikun Chu,¹ Dongping Yang,^{2,3,4,a)} and Xiaodong Huang^{1,a)}



AFFILIATIONS

- Department of Physics, South China University of Technology, Guangzhou 510640, China
- ²Fujian Institute of Research on the Structure of Matter, Chinese Academy of Sciences, Fuzhou 350002, China
- Quanzhou Institute of Equipment Manufacturing, Haixi Institute, Chinese Academy of Sciences, Quanzhou 362200, China
- ⁴School of Physics, University of Sydney, Sydney, New South Wales 2006, Australia

ABSTRACT

Early afterdepolarization (EAD) is a major arrhythmogenic factor in the long QT syndrome (LQTS), whose conditions for genesis have puzzled people for several decades. Here, we employ the phase I Luo-Rudy ventricular myocyte model to investigate EAD using methods from nonlinear dynamics and provide valuable insights into EAD genesis from a physical perspective. Two major results are obtained: (i) Sufficient parametric conditions for EAD are analytically determined and then used to analyze in detail the effects of the physiological parameters. (ii) The normal form of the Hopf bifurcation that leads to EAD is derived and then used to determine whether the Hopf bifurcation is subcritical or supercritical for EAD genesis and the corresponding amplitude and period of the EAD oscillation. Our work here paves the way for further studies of more complicated multi-scale dynamics of EAD and may lead to effective treatments for LQTS arrhythmias.

Published under license by AIP Publishing. https://doi.org/10.1063/1.5133086

Long QT syndrome (LQTS) is a kind of disease with a high risk of causing arrhythmia. It is characterized by an extraordinary prolongation of the QT interval in an electrocardiogram. It is due to the prolongation of the action potential (AP) of the ventricular myocytes. Along with the AP prolongation, a type of triggered activity called early afterdepolarization (EAD) may occur, which appears as a secondary membrane voltage oscillation during the repolarization phase of an AP. It may trigger abnormal excitations in cardiac tissue and, thus, is regarded as one of the major arrhythmogenic factors in LQTS. Several electrophysiological mechanisms have been proposed, but none are fully accepted. The nonlinear dynamics are well understood and supported by electrophysiological experiments. EAD is produced by a dual Hopf-homoclinic bifurcation. This paper explores the sufficient parametric conditions for EAD, which are not yet fully known. Moreover, we consider the normal form of the Hopf bifurcation for EAD, which can reveal the characteristics of the amplitude and period, as this has not yet been derived. Our results shed light on the effects of the parameters on generating and modulating EAD. This work may help in providing a better understanding of the more complicated multi-scale dynamics of EAD and in developing effective treatments for LQTS.

I. INTRODUCTION

Long QT syndrome (LQTS) is a kind of disease with a high risk of causing arrhythmia. QT is defined as the time interval between the beginning of the QRS complex (contraction of the ventricle) and the end of the T wave (repolarization of the ventricle) in an electrocardiogram (ECG). QT is a rough measure of the action potential duration (APD) of the ventricular myocytes. See the normal action potential (AP) and ECG in Fig. 1(a). LQTS is characterized by the extraordinary prolongation of the QT interval, which is actually due to the prolongation of the APD. Along with the APD prolongation, a type of triggered activity called early afterdepolarization (EAD) may occur, 1-3 which is recognized as an oscillation of the secondary membrane voltage during the repolarization phase of an AP [see the red trace in Fig. 1(a)]. Then, in a tissue substrate with dispersed repolarization, the myocytes with EAD may serve as a depolarizing source

a) Author to whom correspondence should be addressed: yangdempe@gmail.com and schuangxd@scut.edu.cn

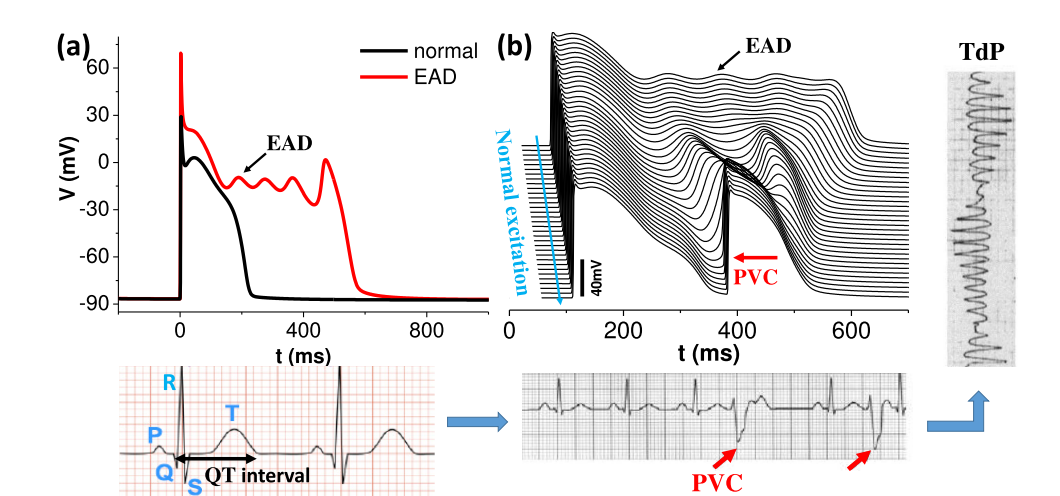


FIG. 1. (a) Example traces of a normal AP and an EAD oscillation. The ECG beneath shows the definition of the QT interval. (b) PVC in a 1D cell cable with dispersed repolarization. From top to bottom, each trace represents the AP of a cell within the cable. Extra contractions were detected in the ECG, as shown by the red arrows. PVCs may be followed by TdP, an ECG for which is shown on the right of (b). The TdP mechanism is not fully clear.

and induce premature ventricular contractions [PVCs; see Fig. 1(b) for a graph and clinical ECG] via a sink–source mismatch or spatial instability. 4–9 PVCs may induce reentry and then the so-called torsade de pointes 9,10 [TdP; see the corresponding ECG on the right of Fig. 1(b)], leading to syncope or fatal fibrillation. However, the detailed mechanism of TdP is not yet clearly known. Therefore, EAD is considered to be the major cause of arrhythmias in LQTS, and its mechanism and treatments are being explored.

In electrophysiology, it is well known that inward currents (e.g., the sodium and calcium currents) depolarize while the outward ones (e.g., the potassium current) repolarize the membrane voltage. Hence, it has been hypothesized that the voltage increase during EAD oscillations is due to a net inward current, which is caused by a reduction of the outward currents or an increase of the inward currents.¹¹ However, the results of some experiments are not consistent with this theory.¹²⁻¹⁴ This challenge could be solved using nonlinear dynamics. In Ref. 15, the authors analyzed a ventricular myocyte model (the phase I Luo–Rudy model¹⁶) using nonlinear dynamics and proposed that EAD emerges via the dual Hopf–homoclinic bifurcation, indicating that the bifurcation requires the conductance and kinetics to satisfy certain conditions. This proposal was later supported by various experimental and theoretical results.^{17,18}

Thus, here we consider some unanswered problems relating to EAD:

- 1. The sufficient parametric conditions leading to EAD are not understood. Note that the Hopf bifurcation is just a necessary rather than a sufficient condition for EAD. For example, the theory of Tran *et al.*¹⁵ has not answered why and how modulations of the channel parameters could lead to or eliminate EAD. The sufficient parametric conditions that would allow us to prevent EAD requires further investigation.
- 2. How the channel conductance and kinetics affect the amplitude and frequency of EAD oscillations is not fully understood. In the Hopf bifurcation theory, only the stability of the equilibrium was analyzed, and the characteristics of the amplitude and period were not addressed. Moreover, in our previous work,¹⁹

- we generally found using several ionic models that an enhancement of the inward currents reduces the EAD amplitude, in contrast with the intuition that the inward currents should facilitate EAD oscillations. Thus, these phenomena need to be explained so that we can develop effective ways to reduce the risk of these arrhythmias.
- 3. Although the essence of the Hopf bifurcation in EAD genesis is known, its normal form has not yet been derived. Each type of bifurcation has a normal form equation describing the dynamical properties around the critical point, which can be derived by a well-developed and detailed procedure. ^{20–22} The procedure has been widely applied to various kinds of complex system, such as the Rayleigh–Bénard convection, ²³ brain dynamics, ²⁴ and the spatiotemporal dynamics of cardiac alternans. ²⁵ The normal form of EAD may provide more insights into its dynamical properties, such as the type of the Hopf bifurcation (subcritical or supercritical), as well as the parametric modulations of the amplitude and period.

In the present paper, we analyze the phase I Luo–Rudy model (LR1)¹⁶ to investigate (i) the sufficient conditions for EAD genesis and (ii) the normal form of the Hopf bifurcation describing the amplitude and frequency around its critical point. Methods from nonlinear dynamics are applied, such as stability analysis, bifurcation theory, and perturbation analysis. Based on the present approach, we can analyze more complex models (e.g., models incorporating intracellular ionic cycling), which may help in exploring practical arrhythmogenesis.

II. MODEL AND METHODS

For the LR1 model, the differential equation of the membrane voltage V is

$$C_m \frac{dV}{dt} = -(I_{\text{Na}} + I_{si} + I_{\text{K}} + I_{K1} + I_b + I_{Kp}),$$

which typically involves three time scales in a normal cardiac AP:

1. The sodium current (I_{Na}) activates and inactivates very rapidly, causing the fast upstroke of the AP.

- 2. The L-type calcium channel (LCC) current (I_{si}) activates and inactivates much more slowly than $I_{\rm Na}$ and has a key role in maintaining the long AP plateau.
- 3. The time-dependent potassium channel (KC) current (I_K) activates even more slowly and eventually overcomes the inward currents, repolarizing the cell back to its resting potential.

During EAD oscillations, $I_{\rm Na}$ and I_{Kp} are close to 0 and ignorable, leading to a four-dimensional system,

$$C_{m} \frac{dV}{dt} = -G_{si} df(V - E_{si}) - G_{K} X_{i}(V) x(V - E_{K})$$
$$-G_{K1} K1_{\infty}(V)(V - E_{K1}) - G_{b}(V - E_{b}) = -I, \quad (1a)$$

$$\frac{dd}{dt} = \frac{d_{\infty}(V) - d}{\alpha \tau_d(V)},\tag{1b}$$

$$\frac{df}{dt} = \frac{f_{\infty}(V) - f}{\beta \tau_f(V)},\tag{1c}$$

$$\frac{dx}{dt} = \frac{x_{\infty}(V) - x}{\gamma \tau_{\nu}(V)}.$$
 (1d)

Note that the above model equations are used in the theoretical analysis. For numerical simulations, $I_{\rm Na}$ is added back to generate an AP, but I_{Kp} is omitted because it has little effect on AP behaviors. We use the model in this way throughout the work, unless specified otherwise.

In the model, V is the transmembrane voltage, d and f are the gating variables of the LCC, x is the gating variable for the KC, C_m is the membrane capacitance and is fixed to be $1~\mu$ F, G and E with subscripts represent the channel conductances and the corresponding Nernst potentials, $X_i(V)$, $K1_\infty(V)$, $y_\infty(V)$ (y represents any gating variable), and $\tau_y(V)$ are functions of V, which are given explicitly in the paper of Luo and Rudy. Finally, α , β , and γ are the coefficients of the corresponding time constants, representing their variability in real myocytes.

The time constant τ_x is much larger than τ_d and τ_f so that the system consisting of Eqs. (1a)–(1c) is regarded as a fast subsystem. Following the method of Keener²⁶ for analyzing the fast–slow dynamics, x can be regarded as the bifurcation parameter. The Hopf bifurcation occurs in the three-variable fast subsystem. By solving the steady state of the fast subsystem and calculating the eigenvalues of the associated Jacobian matrix, the critical condition for the Hopf bifurcation is 15,19

$$H(V,x) = \frac{1}{\tau_f} \left(\frac{1}{\tau_f} - a \right) \left(\frac{1}{\tau_d} - a + s_f c \right)$$

$$+ \frac{1}{\tau_d} \left(\frac{1}{\tau_d} - a \right) \left(\frac{1}{\tau_f} - a - s_d b \right) = 0,$$
 (2)

where $a = \partial I/\partial V$, $b = \partial I/\partial d$, $c = \partial I/\partial f$, $s_d = \partial d_\infty(V)/\partial V$, and $s_f = \partial f_\infty(V)/\partial V$. When H < 0, the stable focus becomes unstable. Equation (2) is valid for the present three-variable subsystem, and it would have to be adapted for more complicated models.

The numerical strategy is as follows. The explicit Euler method is used to simulate Eq. (1a), and the Rush-Larsen method²⁷ is

used for Eqs. (1b)–(1d). The time step is $\Delta t=0.01\,\mathrm{ms}$. A pulse stimulus of 2 ms duration and $30\,\mu\mathrm{A/cm^2}$ magnitude is delivered to excite the cell. The control parameters are $G_{si}=0.13\,\mathrm{ms/cm^2}$, $G_{\rm K}=0.282\,\mathrm{ms/cm^2}$, and $\alpha=\beta=\gamma=1$. The other parameters are the same as those in Ref. 15. Unless specified otherwise, the parameters are set to these control values. Around the bifurcation point, τ_x varies little and can be regarded as a constant so that we set $\tau_x=640\,\mathrm{ms}$.

III. PARAMETRIC CONDITIONS FOR EAD GENESIS

This section investigates the sufficient parametric conditions for EAD, which is one of the targets of the present work.

A. Dynamical description of EAD genesis

We start by briefly introducing a concrete physical description of the EAD dynamics. Since d and f vary fast relative to x and thus can reach their steady states within the period that x remains nearly constant. In this way, the quasi-steady state current (I_{QSS}) of the system can be obtained by setting Eqs. (1b) and (1c) equal to 0, and Eq. (1a) becomes

$$\frac{dV}{dt} = -G_{si}d_{\infty}f_{\infty}(V - E_{si}) - G_{K}X_{i}x(V - E_{K})
- G_{K1}K1_{\infty}(V - E_{K1}) - G_{b}(V - E_{b})
= -I_{OSS}(V, x),$$
(3)

where x is regarded as a time-independent parameter and the function $-I_{QSS}(V,x)$ determines the evolution of V. I_{QSS} is called the central manifold. Its dependence on V at x=0.1 is shown in Fig. 2(a). I_{QSS} has three zeroes, corresponding to three quasi-steady states of the fast subsystem, namely, r, s, and p. r is the homeostasis state, which has nothing to do with EAD, s is the saddle, and p is a focus whose stability depends on x. The dependence of the quasi-steady states on x is shown in Fig. 2(b). As x increases, the p state experiences a Hopf bifurcation and becomes an unstable focus (the uppermost branch transitions from solid to dashed), around which a limit cycle is formed and EAD can emerge. The bifurcation point is denoted as p^* . As x increases further, s and p collide and annihilate via a saddle-node bifurcation.

Figure 2(a) is actually the nullcline of the fast subsystem, whereas the nullcline of the slow subsystem can be obtained by setting Eq. (1d) equal to 0, leading to $x = x_{\infty}(V)$, as shown by the cyan curves in Figs. 2(c), 2(e), and 2(g). The intersections of these two nullclines are the steady states of the whole system. The steady states on the branches p and r are always stable and that on branch s is unstable. Only the steady state on branch p is relevant, and it is labeled q in Fig. 2 as it represents the global steady state of the whole system.

Now, we can introduce the dynamical diagram of the whole system based on the properties of the fast subsystem and the relative positions of p^* and q, as well as the orbit of AP. In the coordinate space (x, V), we denote p^* as (x_{p^*}, V_{p^*}) , and the orbit of AP as the function x(V), where V evolves with time. There are three dynamical scenarios relevant to EAD, as discussed in detail in the following.

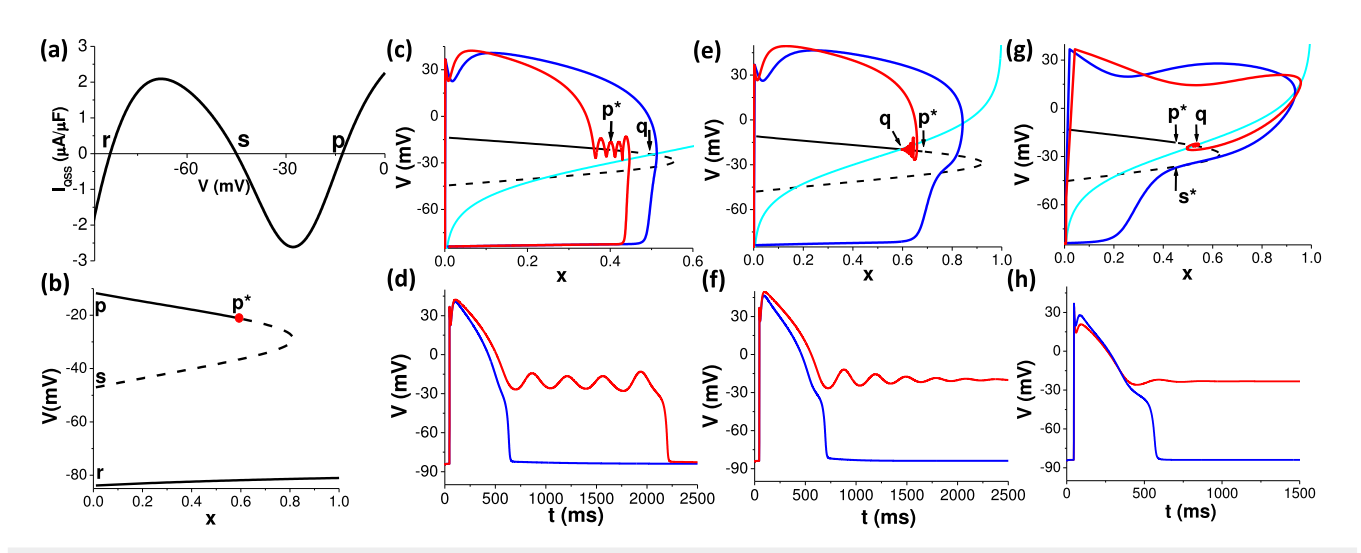


FIG. 2. Scenarios for different AP behaviors (generated by the LR1 model). (a) I_{QSS} as a function of V. $G_{si}=0.165$, x=0.1. (b) The nullcline of the fast subsystem. $G_{si}=0.165$. p^* denotes the bifurcation point. (c) and (d) EAD. The cyan curve is $x=x_{\infty}(V)$. $G_{si}=0.13$. $\gamma=4.1$ and 2 for the red and blue traces, respectively. (e) and (f) The genesis of RF $_{p}$. $G_{si}=0.18$. $\gamma=2$ and 0.8 for the red and blue traces, respectively. (g) and (h) The genesis of RF $_{s}$. $G_{si}=0.14$. $\gamma=0.138$ and 0.06 for the red and blue traces, respectively. S^* is the point right beneath S^* 0 or branch S^* 1.

1. Scenario 1: EAD oscillations

Figure 2(c) presents two possible orbits passing the p branch. The red trace enters the basin of p before it bifurcates so that it is attracted to the stable focus and ramps on branch p until it experiences a Hopf bifurcation at p^* to generate EAD. The blue trace reaches p after the bifurcation so that it is repelled by the unstable focus and thus, EAD does not occur. The corresponding APs are plotted in Fig. 2(d). In this scenario, q is on the unstable section of branch p. EAD genesis requires that q is on the right of p^* , while the AP orbit should reach p before it bifurcates. As a result, the sufficient condition for EAD can be expressed as

$$x_{\infty}(V_{p^*}) > x_{p^*}$$
 and $x(V_{p^*}) < x_{p^*}$. (4)

2. Scenario 2: Repolarization failure due to the p state

Here, q is on the stable section of branch p, as shown in Fig. 2(e), which also shows two orbits. The red one reaches branch p before it bifurcates and resides at the q state permanently, resulting in repolarization failure (RF). The blue one passes branch p via its unstable section and, thus, shows normal repolarization (NR). See the corresponding APs in Fig. 2(f). The condition for the emergence of this scenario is that q and the AP orbit should both be on the left of p^* . Therefore, the sufficient condition for RF due to the p state (RF $_p$) is

$$x_{\infty}(V_{p^*}) \le x_{p^*}$$
 and $x(V_{p^*}) < x_{p^*}$. (5)

3. Scenario 3: RF due to the saddle s

This scenario happens in a system with small γ , where the gate x varies fast. Therefore, the orbit evolves much faster along the x-axis and may escape the basin of the p state and enter the manifold

regime of the saddle s. Then, the orbit may proceed in two possible ways. One is toward the resting state r, leading to NR, which is presented as the blue traces in Figs. 2(g) and 2(h). The other one is toward the q state, where it stays permanently, resulting in RF due to the saddle s (RF $_s$), shown as the red traces. This scenario is irrelevant to p^* . The critical state between NR and RF $_s$ is when the orbit just reaches the point right beneath p^* on branch s [denoted as s^* in Fig. 2(g)], i.e., $x(V_{s^*}) = x_{p^*}$. If the orbit passes through the above of s^* , RF $_s$ occurs. Hence,

$$x(V_{s^*}) < x_{p^*} \tag{6}$$

is a sufficient condition for RF_s.

In the following, we will analytically find concrete expressions for Eqs. (4)–(6), which naturally lead to the parameter constraints for the various dynamical scenarios.

B. Parameter constraints

Although the parameter constraints can be directly explored by brute numerical simulations, more insights can be gained from an analytically closed form. In the present work, approximations are employed to simplify the formulations (Appendix A), rendering the analytically closed form available. In the following, we consider two kinds of parameters: (i) the ionic conductances and (ii) the kinetics of LCC (i.e., α and β).

1. The ionic conductances

Here, we consider only the conductance parameters G_{si} and G_{K} , which are known to be responsible for EAD dynamics. α and β are fixed at 1.

2. Scenario 1: EAD

The condition for this scenario is given in Eq. (4), which requires expressions for (i) the Hopf bifurcation point (x_{p^*}, V_{p^*}) and (ii) the AP orbit x(V). These are derived as follows.

First, by approximating the nonlinear functions as polynomials and employing the Lagrangian interpolation method, 28 p^* can be found directly from Eq. (2) and expressed as the following form:

$$V_{p^*} = A_2 G_{si}^2 + A_1 G_{si} + A_0,$$

$$x_{p^*} = \frac{B_2 G_{si}^2 + B_1 G_{si} + B_0}{G_Y}.$$
(7)

A detailed calculation for A_n and B_n (n = 0, 1, 2) is given in Appendix A.

Second, the orbit of the whole system in the *x* vs *V* phase plane is determined by the following two dynamical equations:

$$\frac{dx}{dt} = \frac{x_{\infty}(V) - x}{v \tau_{v}}, \quad \frac{dV}{dt} = -I,$$

where $\tau_x = 640$ ms and $x_{\infty}(V)$ can be approximated as a linear function of V, since it appears as a straight line around q [Fig. 2(c)], i.e., $x_{\infty} = mV + n$ with m = 0.0186 and n = 0.96, leading to

$$\frac{dx}{dV} = \frac{mV + n - x}{-I\gamma\tau_{r}}. (8)$$

As EAD occurs around branch p where the ionic current is close to 0, -I can be linearly approximated as $I_p(V_p)$ (by a Taylor expansion)

$$-I(V) \approx I_{p}(V_{p})$$

$$= -I[V_{p} + \delta V, d_{\infty}(V_{p}) + \delta d, f_{\infty}(V_{p}) + \delta f]$$

$$= -I[V_{p}, d_{\infty}(V_{p}), f_{\infty}(V_{p})]$$

$$-\frac{\partial I}{\partial V}\Big|_{p} \delta V - \frac{\partial I}{\partial d}\Big|_{p} \delta d - \frac{\partial I}{\partial f}\Big|_{p} \delta f$$

$$= -a\delta V - b\delta d - c\delta f, \tag{9}$$

where δV , δd , and δf are small constant deviations from the quasisteady state p. Thus, Eq. (8) becomes a linear differential equation. It describes the orbit near V_p and its solution is

$$x(V) = mV + n - mF_p + (x_0 - mV_0 - n + mF_p)e^{-(V - V_0)/F_p}, (10)$$

where $F_p = I_p(V_p)\gamma \tau_x$ and V_0 and x_0 are the initial values of V and x, respectively. Since x(V) is solved around the p state, the initial state should vary with p. Thus, it is reasonable to take $x_0 = x_p - \Delta x$ and $V_0 = V_p - \Delta V$ with Δx and ΔV being constants. As a result, x(V) becomes

$$x(V) = mV + n - mF_{p} + [(x_{p} - \Delta x) - m(V_{p} - \Delta V) - n + mF_{p}]e^{-(V - V_{p} + \Delta V)/F_{p}}.$$
(11)

By substituting $V=V_p=V_{p^*}$ and $x_p=x_{p^*}$ into Eq. (11) and using $x_\infty=mV+n$, the condition Eq. (4) for EAD genesis becomes

$$x_{\infty}(V_{p^*}) > x_{p^*}, \tag{12}$$

$$x_{p^*} > x_1, \tag{13}$$

with

$$x_{\infty}(V_{p^*}) = m(A_2G_{si}^2 + A_1G_{si} + A_0) + n, \tag{14}$$

$$x_1 = m(V_{p^*} - F_{p^*}) + n + \frac{(-\Delta x + m\Delta V)e^{-\Delta V/F_{p^*}}}{1 - e^{-\Delta V/F_{p^*}}},$$
 (15)

where $F_{p^*} = I_{p^*} \gamma \tau_x$ with $I_{p^*} = I_p(V_{p^*})$, which is independent of G_K . Thus, x_1 is a function of G_{si} and γ , and it is independent of G_K .

3. Scenario 2: RFp

The condition for this scenario requires the simultaneous ful-fillment of Eq. (13) and

$$x_{\infty}(V_{p^*}) \le x_{p^*},\tag{16}$$

with $x_{\infty}(V_{p^*})$ being given by Eq. (14).

4. Scenario 3: RFs

This scenario relies on the condition in Eq. (6). $x(V_{s^*})$ can be obtained by replacing V_p and F_p with V_s and $F_s = I_s(V_s)\gamma \tau_x$ in Eq. (11), respectively, and substituting $x = x_{p^*}$ and $V = V_s = V_{s^*}$ into Eq. (11). In this way, Eq. (6) becomes

$$x_{p^*} > x_2, \tag{17}$$

with

$$x_2 = m(V_{s^*} - F_{s^*}) + n + \frac{(-\Delta x + m\Delta V)e^{-\Delta V/F_{s^*}}}{1 - e^{-\Delta V/F_{s^*}}},$$
 (18)

which is a function of V_{s^*} and also independent of G_K . V_{s^*} can be solved by setting $I_{QSS} = 0$ in Eq. (3) and using x_{p^*} from Eq. (7).

5. The kinetics

We need to express x_{p^*} and V_{p^*} as functions of the kinetic parameters. G_{si} and G_K are fixed to the control values. Following the same method used for the conductances, the Hopf bifurcation point can be given as

$$V_{p^*} = C_2 \beta^2 + C_1 \beta + C_0,$$

$$x_{p^*} = D_2 \beta^2 + D_1 \beta + D_0,$$
(19)

where C_n and D_n (n = 0, 1, 2) are functions of α . Their formulations are given in Appendix A.

C. Effects of the parameters on the AP behavior

Some important effects of the parameters can be explained and predicted based on the above analytically closed forms for various scenarios. The relevant discussions are as follows.

1. G_{si} threshold for EAD genesis

In the early EAD theory,^{1,11} it was hypothesized that EAD is due to a net inward current. Accordingly, one would expect that

even though the inward current is small, as long as the outward one is smaller than it, EAD would occur. However, the present theory indicates that there is a lowest threshold calcium current for EAD, as directly indicated by Eq. (7). As $x_{p^*} > 0$ must always be satisfied, we have

$$G_{si} > G_{si,c1}, \tag{20}$$

with

$$G_{si,c1} = \frac{-B_1 + \sqrt{B_1^2 - 4B_2B_0}}{2B_2}. (21)$$

For the control parameter set, $G_{si,c1} = 0.059$, approximating well the numerical result 0.061. Figure 3(a) is the G_{si} vs γ phase diagram. The green dashed vertical line indicates the lowest G_{si} for EAD. If $G_{si} < G_{si,c1}$, EAD is definitely prevented. Note that the threshold LCC conductance $G_{si,c1}$ is irrelevant to the KC conductance, and this property is universal in other models (see the results shown in Figs. 10–14 in Appendix C). Based on the finding for $G_{si,c1}$, we suggest that a specific drug that uniquely reduces the LCC conductance may prevent EAD.

2. Requirement of γ for EAD genesis

If $G_{si} > G_{si,c1}$, EAD and RF_p can occur. From Eqs. (12) and (13), we see that EAD requires $x_1 < x_{p^*} < x_{\infty}(V_{p^*})$, i.e.,

$$x_1 < \frac{B_2 G_{si}^2 + B_1 G_{si} + B_0}{G_K} < m(A_2 G_{si}^2 + A_1 G_{si} + A_0) + n.$$
 (22)

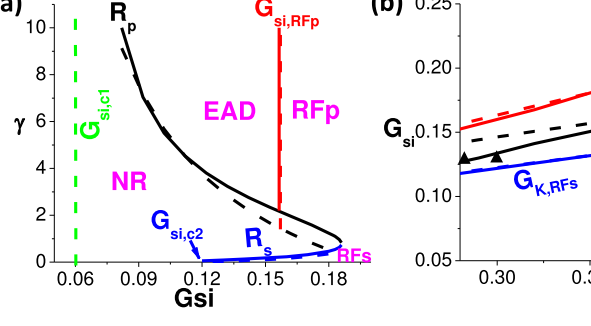
Here, x_1 is a function of γ and G_{si} , as expressed by Eq. (15). The solutions for γ and G_{si} are given by

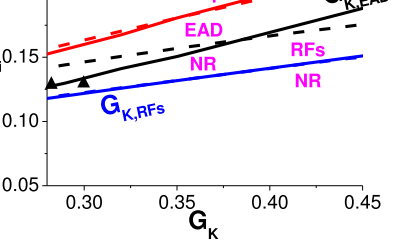
$$\gamma > R_p$$
 and $G_{si} < G_{si,RFp}$, (23)

with

$$R_p = \frac{\Delta V}{I_{p^*} \tau_x \ln[1 + (m\Delta V - \Delta x)/(x_{p^*} - m(V_{p^*} - F_{p^*}) - n)]}, (24)$$

$$\frac{1}{(p^* - F_{p^*}) - n)},$$
 (24)





0.9

FIG. 3. Parametric conditions for the AP behaviors. The parameters shown on the axes were scanned and the others were set to their control values. The solid and dashed curves represent the simulated and theoretical results, respectively. The black, red, and blue curves represent the critical conditions for EAD, RF_D, and RF_S, respectively, the functions of which are denoted beside the curves in the corresponding colors. (a) G_{si} vs γ phase diagram. (b) G_K vs G_{si} . (c) β vs α . In (b) and (c), RF_s and the other two states (EAD and RF_p) appear at different values of γ , as indicated in Table I. Each theoretical curve requires five parameters to be determined: $(\delta V, \delta d, \delta f, \Delta V, \Delta x)$. Here, δV is fixed to be -0.2 mV, and all the other parameter values are listed in Table I. The two black triangles in (b) denote the parameter sets that we select to plot typical APs, which are shown in Fig. 15(a) in Appendix C.

$$G_{si,RFp} = \frac{-T + \sqrt{T^2 - 4K}}{2},$$
 (25)

where

$$T = \frac{B_1 - mG_K A_1}{B_2 - mG_K A_2}$$

and

$$K = \frac{B_0 - mG_K A_0 - nG_K}{B_2 - mG_K A_2}.$$

 R_p depends on I_{p^*} , x_{p^*} , and V_{p^*} , which are functions of G_{si} and G_K . Thus, it is a function of G_{si} and G_K . $G_{si,RFp}$ is a function of G_K . Therefore, if γ is larger than a certain value of R_p , then EAD could occur. For given G_K , R_p depends only on G_{si} , which is plotted in Fig. 3(a) as a black dashed curve. Moreover, given GK, Gsi,RFp becomes a constant. For the control set, it is 0.155, plotted in Fig. 3(a) as the red dashed line. We can see that the theoretical results coincide with the numerical ones satisfactorily. Equation (23) provides a theoretical estimate of the threshold γ of EAD for different parameter sets.

3. Calcium and potassium conductance constraints for EAD genesis

If G_K and G_{si} satisfy certain constraints, then EAD occurs. The constraints are derived as follows. Here, Eq. (22) leads to

$$G_{K,RFp} < G_K < G_{K,EAD}, \tag{26}$$

where

$$G_{K,RFp} = \frac{B_2 G_{si}^2 + B_1 G_{si} + B_0}{m(A_2 G_{ci}^2 + A_1 G_{si} + A_0) + n},$$
(27)

TABLE I. Values of γ , δd , δf , ΔV , and Δx for each panel in Fig. 3. They were determined somewhat empirically, but the qualitative results are robust against their values if they satisfy specific conditions, which are given in Appendix B. Note that the boundary for scenario 2 (the red curve for RF_p) is independent of these parameters and is given by Eqs. (25), (27), and (39).

	Scenario 1 (the black curve)					Scenario 3 (the blue curve)				
	γ	δd	δf	ΔV	Δx	γ	δd	δf	ΔV	Δx
A		0.05	-0.085	-24	0.0128		0.078	-0.295	-0.2	-0.006
В	3.5	0.012	-0.022	-18	0.018	0.04	0.079	-0.28	-0.8	-0.001
C	5	-0.05	0.012	-20	0.021	0.5	-0.05	0.02	-0.72	-0.0018

$$G_{K,EAD} = \frac{B_2 G_{si}^2 + B_1 G_{si} + B_0}{x_1}.$$
 (28)

That means for a given G_{si} , G_K should be within a certain range to cause EAD.

On the other hand, when G_K is given, Eq. (26) becomes

$$G_{si,EAD} < G_{si} \le G_{si,RFp},$$
 (29)

where $G_{si, EAD}$ is a complex function of γ and G_K and needs to be determined numerically. Therefore, for EAD genesis, G_{si} and G_K should simultaneously satisfy

$$G_{si,EAD} < G_{si} < G_{si,RFp},$$

 $G_{K,RFp} < G_{K} < G_{K,EAD}.$ (30)

That means the calcium and potassium currents should match in an appropriate range to give rise to EAD. In Fig. 3(b), we plot $G_{K,EAD}$ and $G_{K,RFp}$ as functions of G_{si} , shown as the black and red dashed curves, respectively. If we were to plot $G_{si,EAD}$ and $G_{si,RFp}$ as functions of G_K , we would get the same black and red dashed curves. Therefore, violation of Eq. (30) can effectively prevent EAD. Thus, in the EAD state, a decrease of G_{si} or an increase of G_K would return the myocyte to NR. On the other hand, an increase of G_{si} or a reduction of G_K that is too large may result in RF_p .

Exposure to isoproterenol can increase both the LCC and KC conductances simultaneously, which may trigger EAD, ^{29,30} which is responsible for the arrhythmogenesis of type 2 LQTS. Equation (30) can explain this phenomenon. We hypothesize that any drug with a similar effect may induce EAD. This finding may be useful for evaluating drug effects.

4. Parametric condition for RFs

This behavior is seldom described in previous studies. It generally exists in various myocyte models when the kinetics of KC (referred to as the Ks channel in other models) becomes fast, i.e., γ is small, as is shown in Figs. 10–14 in Appendix C.

First, just like EAD, there is a preliminary condition for the occurrence of RF_s. Here, $\gamma > 0$ so that $\gamma \to 0$ ($F_{s^*} \to 0$) is the limit case for RF_s. Since we have

$$\lim_{F_{s^*}\to 0} \frac{n + (-\Delta x + m\Delta V - n)e^{-\Delta V/F_{s^*}}}{1 - e^{-\Delta V/F_{s^*}}} - mF_{s^*} = n.$$

Equation (17) implies

$$x_{p^*} \ge mV_{s^*} + n. \tag{31}$$

This is the preliminary condition for RF_s. Thus, $G_{si} \ge G_{si,c2} = 0.1167$ when the other parameters are set to their defaults [denoted by the blue arrow in Fig. 3(a)]. This value coincides perfectly with the simulated value of 0.1161.

If $G_{si} \ge G_{si,c2}$, the occurrence of RF_s requires $x_{p^*} > x_2$, i.e.,

$$\frac{B_2 G_{si}^2 + B_1 G_{si} + B_0}{G_K} > x_2, (32)$$

where x_2 is a function of γ and G_{si} [Eq. (18)]. Thus, we have

$$\gamma < R_s,$$
 (33)

where

$$R_{s} = \frac{\Delta V}{I_{s^{*}} \tau_{x} \ln[1 + (m\Delta V - \Delta x)/(x_{p^{*}} - m(V_{s^{*}} - F_{s^{*}}) - n)]}.$$
 (34)

Moreover, from Eq. (32), we get

$$G_{\rm K} < G_{\rm K,RFs},\tag{35}$$

where

$$G_{K,RFs} = \frac{B_2 G_{si}^2 + B_1 G_{si} + B_0}{x_2}. (36)$$

 R_s and G_{K,RF_s} are plotted as the dashed blue curves in Figs. 3(a) and 3(b) as functions of G_{si} . The analytical results coincide well with the numerical ones. Hence, a decrease of G_{si} , an increase of G_K , and an increase of γ can violate Eqs. (32), (33), and (35), respectively, so can prevent RF_s. In a real ventricle, RF_s may result in an ultralong AP, which exacerbates the repolarization heterogeneity of the tissue substrate, 31,32 increasing the risk of PVC. Our findings for RF_s may help in controlling the ultralong AP.

5. Effects of the kinetics

Before the EAD bifurcation theory was proposed, the influence of the kinetics was seldom considered. Here, we explicitly discuss the dependence of EAD genesis on the kinetics.

For EAD genesis, Eqs. (12) and (13) imply

$$x_1 < D_2\beta^2 + D_1\beta + D_0 < m(C_2\beta^2 + C_1\beta + C_0) + n,$$
 (37)

which gives

$$\beta_{\text{RF}p} < \beta < \beta_{\text{EAD}},$$
(38)

where

$$\beta_{\text{RF}p} = \frac{-T + \sqrt{T^2 - 4K}}{2} \tag{39}$$

and where

$$T = \frac{D_1 - mC_1}{D_2 - mC_2}$$

and

$$K = \frac{D_0 - mC_0 - n}{D_2 - mC_2}.$$

Here, β_{EAD} is a complex function of α , and it needs to be determined numerically.

The condition for RF_s is

$$D_2\beta^2 + D_1\beta + D_0 > x_2, (40)$$

which gives

$$\beta < \beta_{RFs}$$
. (41)

Here, $\beta_{\rm RFs}$ is a function of α and needs to be determined numerically. $\beta_{\rm EAD}$, $\beta_{\rm RFp}$, and $\beta_{\rm RFs}$ are plotted as black, red, and blue dashed curves in Fig. 3(c), respectively. Therefore, an increase of β violates Eqs. (38) and (41) and may turn EAD and RF $_{\rm S}$ into NR. α must have the opposite effect as β because β is in the numerators of Eq. (19), whereas α is in the denominators [also see Eq. (A6) in Appendix A] so that β and α modulate V_{p^*} and x_{p^*} conversely as well as the AP behaviors.

6. Role of the initial state

The AP orbit depends on the initial state (V_0 , x_0), as shown by Eq. (10). Thus, it may alter the AP behavior, which suggests a potential way for controlling the relevant arrhythmogenesis. In this part, we discuss the role of the initial state in generating the arrhythmogenic AP behaviors.

First, we will analyze EAD. From Eq. (10), we get

$$\frac{dx(V_{p^*})}{dV_0} = \frac{e^{-(V_{p^*} - V_0)/F_{p^*}}}{F_{p^*}} (x_0 - mV_0 - n) > 0,$$

$$\frac{dx(V_{p^*})}{dx_0} = e^{-(V_{p^*} - V_0)/F_{p^*}} > 0,$$

$$\frac{dx_{p^*}}{dV_0} = \frac{dx_{p^*}}{dx_0} = 0.$$
(42)

The reasons for the inequalities are

- 1. The point (x_0, V_0) must be on the left of the x_∞ curve for EAD [Fig. 2(c)] so that $x_0 < x_\infty(V_0) = mV_0 + n$.
- 2. V repolarizes until it reaches p^* so that $dV/dt=-I\approx I_{p^*}<0$, and thus, $F_{p^*}=I_{p^*}\gamma \tau_x<0$.

Therefore, any perturbation reducing V_0 or x_0 before the plateau phase of an AP can reduce $x(V_{p^*})$, leading to $x(V_{p^*}) < x_{p^*}$ [i.e., Eq. (4)], as well as EAD. Figure 4(a) shows an example AP trace with a transition from NR to EAD due to a negative voltage perturbation.

For RF_s, we get

$$\frac{dx(V_{s^*})}{dV_0} = \frac{e^{-(V_{s^*} - V_0)/F_{s^*}}}{F_{s^*}} (x_0 - mV_0 - n) < 0,$$

$$\frac{dx(V_{s^*})}{dx_0} = e^{-(V_{s^*} - V_0)/F_{s^*}} > 0.$$
(43)

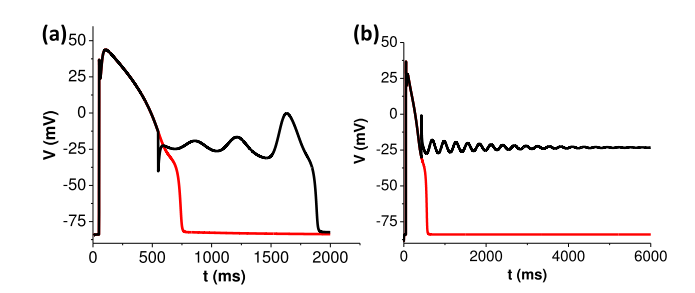


FIG. 4. Influence of a perturbation on AP. (a) A negative perturbation of V transforms NR into EAD. $G_{si}=0.142$ and $\gamma=2.4$. The perturbation is an instant pulse with a magnitude of -27.7 mV. (b) A positive perturbation transforms NR into RF $_s$. $G_{si}=0.14$ and $\gamma=0.14$. The pulse magnitude is 20 mV.

In this case,

- 1. (x_0, V_0) must be on the right of the x_∞ curve as it approaches s^* [Fig. 2(g)] so that $x_0 > mV_0 + n$.
- 2. V repolarizes to approach s^* so that $dV/dt = -I \approx I_{s^*} < 0$, and thus, $F_{s^*} = I_{s^*} \gamma \tau_x < 0$.

Hence, an increase of V_0 or a decrease of x_0 can reduce $x(V_{s^*})$, facilitating $x(V_{s^*}) < x_{p^*}$ [i.e., Eq. (6)], as well as RF_s. Figure 4(b) shows the effect of a positive voltage perturbation that transforms NR into RF_s.

It might seem that an increase of the voltage should facilitate EAD, while a reduction would eliminate it. However, the theory indicates the reverse. It has been reported that an increase of the transient outward current (I_{to}) promotes EAD oscillations.^{12,19} The puzzle is that I_{to} is an outward current, which tends to reduce the voltage. The present theory provides a general and explicit explanation for this. When I_{to} flows outward, V_0 may be reduced, facilitating EAD. Therefore, a perturbation delivered to the voltage (e.g., an electric shock by an implanted defibrillator) or the KC gate (e.g., a specific neurotransmitter) may transition an abnormal EAD or RF state into a NR state, implying a potential method of treating EAD.

In summary, the conditions for the dynamical behaviors relevant to EAD are listed in Table II. We stress that the present theory is a phenomenological one. Its significance is that it reveals the parametric dependence of the genesis of various arrhythmogenic behaviors. The generality of our analytical results is verified by the updated myocyte models (shown in Appendix C). Therefore, the present analytical conditions can be used to interpret the EAD arrhythmogenesis and suggest treatments.

IV. THE NORMAL FORM OF EAD

The general normal form for the Hopf bifurcation is

$$\frac{dz}{dt} = (\lambda + i\omega_0)z + c|z|^2 z + O(|z|^3), \tag{44}$$

where z is a complex number describing the amplitude and frequency of the limit cycle around the bifurcation point, λ is the largest real part of the eigenvalue near the critical point, ω_0 is the intrinsic oscillatory frequency exactly at the critical point, and c is a model-dependent coefficient determining whether the Hopf bifurcation

TABLE II. Sufficient conditions for the various AP behaviors, organized hierarchically. For example, the occurrence of EAD first requires $G_{si} > G_{si,c1}$, $x_{p^*} < x_{\infty}(V_{p^*})$, and $x_{p^*} > x(V_{p^*})$. If all three conditions are satisfied, then EAD occurs.

$G_{si} > G_{si,c1}$ $x_{p^*} < x_{\infty}(V_{p^*})$	$x_{p^*} > x_{\infty}(V_{p^*})$:)							
	$x_{p^*} > x_{\infty}(V_{p^*})$	1)							
$x_{p^*} > x(V_{p^*})$ $x_{p^*} \le x(V_{p^*})$ $x_{p^*} >$	$x(V_{p^*}) \qquad x_{p^*}$	$\leq x(V_{p^*})$							
EAD NR I	RF_p	NR							
$x_{p^*} \ge mV_{s^*} + n$									
$x_{p^*} > x(V_{s^*})$	$x_{p^*} < x(V_{s^*})$								
RF_s	NR								

is subcritical [Re(c) > 0] or supercritical [Re(c) < 0]. The detailed derivation of Eq. (44) for the LR1 model is cumbersome and can be found in the supplementary material.

Since $|z| \ll 1$, then $O(|z|^3)$ can be omitted. Let $z = Ae^{i\omega}$, where A (a real number) denotes the amplitude and ω represents the frequency around the critical point. Thus, Eq. (44) becomes

$$\frac{dA}{dt} = \lambda A + \operatorname{Re}(c)A^{3},\tag{45}$$

$$\omega = \omega_0 + \operatorname{Im}(c)A^2,\tag{46}$$

whose steady solution for A is given by dA/dt = 0, leading to

$$A = \sqrt{-\lambda/\operatorname{Re}(c)},\tag{47}$$

in which $\lambda<0$ is required for the subcritical bifurcation and $\lambda>0$ for the supercritical one. It can be easily verified that this solution is unstable in the subcritical case, which would grow to infinity. Thus, in this case, the negative higher-order term needs to be included, and Eq. (45) should be replaced by

$$\frac{dA}{dt} = \lambda A + \operatorname{Re}(c)A^{3} - \operatorname{Re}(g)A^{5}, \tag{48}$$

where Re(g) > 0 to confine A, leading to a stable limit cycle with amplitude

$$A^{2} = \left[1 + \sqrt{1 + \frac{4\operatorname{Re}(g)\lambda}{\operatorname{Re}(c)^{2}}}\right] \frac{\operatorname{Re}(c)}{2\operatorname{Re}(g)}$$

$$\approx \frac{\operatorname{Re}(c)}{\operatorname{Re}(g)} + \frac{\lambda}{\operatorname{Re}(c)} \quad (\lambda \ll 1)$$
(49)

coexisting with the stable equilibrium. Thus, a bistable region is formed. Typical examples of the two types of bifurcation are shown in Fig. S1 in the supplementary material. Based on the analyses of the normal form, we discuss two problems in Secs. IV A and IV B.

A. The type of the Hopf bifurcation

What type of Hopf bifurcation is EAD? This has not yet been answered by the theory of Tran *et al.*.¹⁵ We numerically calculate Re(c) by using the approximate polynomials in the model to identify

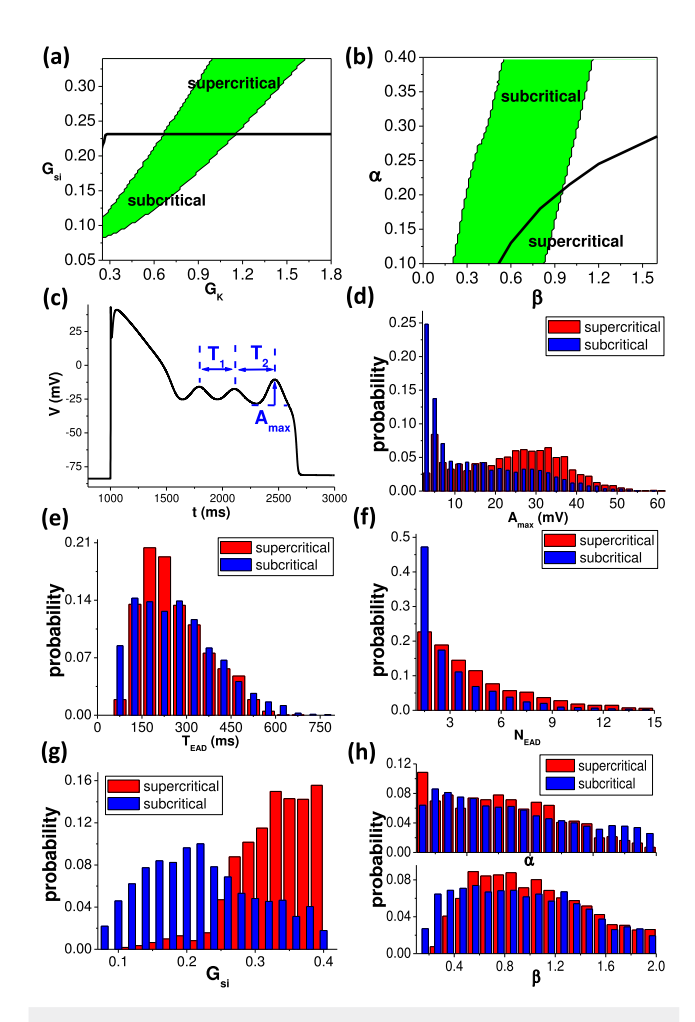


FIG. 5. Bifurcation types and the corresponding development of EAD. $\gamma=10$. (a) $\alpha=\beta=1$. The EAD regions are green. (b) $G_{si}=0.13$ and $G_K=0.282$. (c) Definitions of the maximum amplitude and the inter-EAD period within an AP. Each bump is counted as one instance of EAD, and the time interval between successive bumps is the inter-EAD period, denoted as T_1 , T_2 , etc. (d)–(f) Probability distributions of the maximum amplitude, the inter-EAD period, and the number of EAD occurrences, respectively. The parameters are assigned randomly within certain ranges, as stated in the text. (g) and (h) The dependence of the bifurcation type on the parameters. The upper and lower histograms in (h) are for α and β , respectively.

the bifurcation type. In the G_K vs G_{si} plane, we can see that large G_{si} yields the supercritical Hopf bifurcation, while G_K has little effect on changing the bifurcation type [Fig. 5(a)]. The β vs α plane is shown in Fig. 5(b). The bifurcation type is not only a problem of theoretical interest but also has medical significance. We can see that the EAD amplitude and period, which are closely related to PVC and the diagnosis of EAD using an ECG, are correlated with the bifurcation type. Therefore, the association between the bifurcation type and the EAD characteristics needs to be elucidated.

We gathered data for the maximum EAD amplitude (A_{max}) , the inter-EAD period (T_i) , and the number of occurrences of the

EAD oscillation ($N_{\rm EAD}$) separately for the sub- and supercritical bifurcations. The definitions of the above quantities in an AP are shown in Fig. 5(c). The APs were generated by randomly assigning values to the four investigated parameters within certain ranges: $G_{si} \in (0.07, 0.4)$, $G_{\rm K} \in (0.1, 3.0)$, $\alpha \in (0.1, 2)$, and $\beta \in (0.1, 2)$. Only the APs with EADs were used, rather than those with NR and RF. They were classified as sub- or supercritical depending on Re(c). The distribution histograms are shown in Figs. 5(d)–5(f). We can see that the maximum amplitude for the supercritical bifurcations is larger than for the subcritical bifurcations, whereas there is no evident difference in their periods. The distribution of EAD occurrences for the subcritical bifurcations is a little bit steeper than for supercritical bifurcations, indicating that there were fewer EAD occurrences for subcritical bifurcations.

The above phenomena can be explained as follows. First, we see from Figs. 5(g) and 5(h) that G_{si} is the deterministic parameter for causing the bifurcation type to change, whereas G_K , α , and β have much less influence. These figures show the dependence of the bifurcation type individually for the three parameters. The distributions of G_{si} are very different for sub- and supercritical bifurcations, whereas those for α and β show much less difference. Therefore, the bifurcation type depends mostly on G_{si} .

Next, we consider the nullcline of the fast subsystem, as shown in Fig. 2(b) and the inset of Fig. 9(a) in Appendix B. As G_{si} becomes larger, the unstable section of branch p (the dashed section) is prolonged, and the mouth within branches p and s is enlarged [Fig. 9(a), inset]. The unstable section of branch p allows for EAD oscillations. As this section gets longer, more EAD events can occur within it, and thus, a larger amplitude may develop. Therefore, the supercritical EADs have larger maximum amplitudes and more occurrences of oscillation. Thus, we suggest that supercritical EADs

at high calcium conductance may have a higher risk of inducing PVCs.

B. Influence of the parameters on the EAD amplitude and period

First, we investigate the amplitude modulation based on Eq. (45). To reveal the effects of the individual parameters on the amplitude, we fix *x* to x_f and calculate λ (let $x_f > x_{p^*}$ so that $\lambda > 0$). Figure 6 shows λ and Re(c) and the resulting amplitude A^2 . Note that for the subcritical bifurcation, $\lambda / \operatorname{Re}(c)$ is plotted instead of $\operatorname{Re}(c)/\operatorname{Re}(g) + \lambda/\operatorname{Re}(c)$ to represent A^2 . This is because it is very difficult to determine the coefficient Re(g) of the higher-order term in Eq. (49), whereas Re(c)/Re(g) does not change much. Therefore, $\lambda / \operatorname{Re}(c)$ approximately indicates the variation of the amplitude. The data around the lines separating the two types of bifurcation are discarded because near these lines, Re(c) is very close to 0 and the amplitude would approach infinity in theory. In this case, higherorder terms would reduce the amplitude, but these have not been taken into account in the present work. We can see that as G_{si} and α increase, the amplitude falls [see Figs. 6(a) and 6(c)]. In contrast, as G_K and β increase, the amplitude rises [see Figs. 6(b) and 6(d)]. The physical mechanism may be interpreted as follows. As any parameter is varied, if x_{p^*} is increased, the fixed reference point x_f would become closer to x_{p^*} and λ would decrease, whereas if x_{p^*} is decreased, λ would be increased. On the other hand, the variation of Re(c) is several orders of magnitude smaller than that of λ . So, λ basically determines the variation of the amplitude. Hence, an increase of G_{si} or α would increase x_{p^*} , resulting in a decrease of the amplitude. In contrast, an increase of G_K or β would decrease x_{p^*} and have the opposite effect.

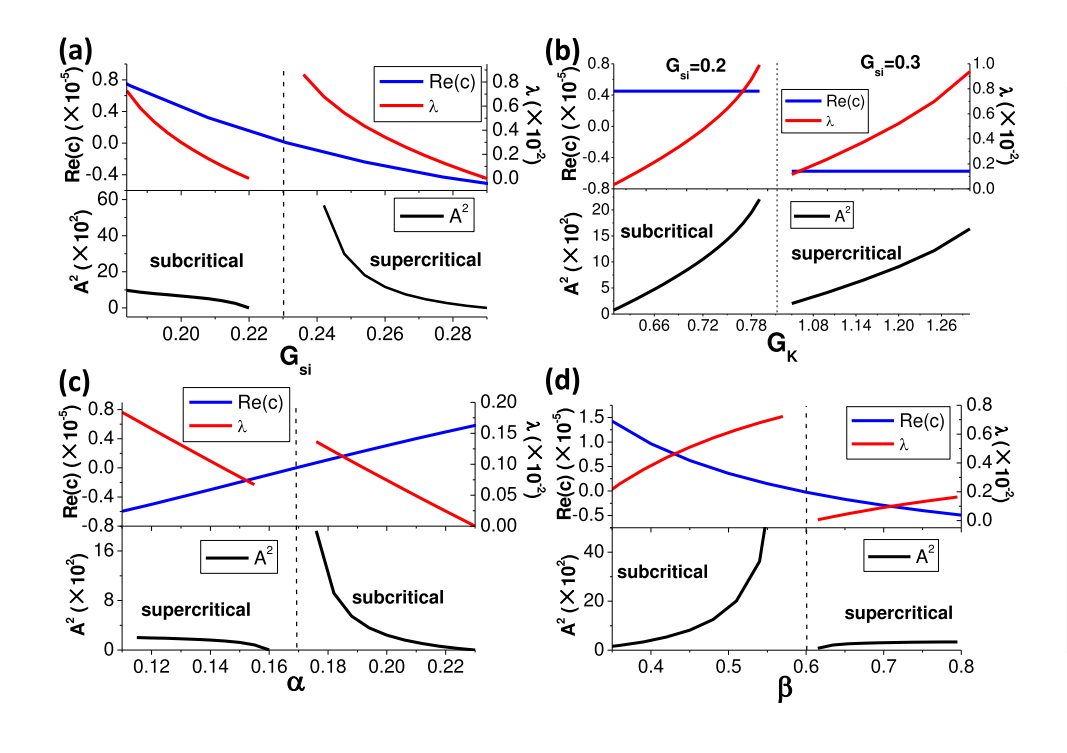


FIG. 6. Parametric modulation of the EAD amplitude as theoretically revealed by the normal form. In each panel, the upper traces are Re(c) and λ , whereas the lower trace is the amplitude from the normal form. λ was calculated using constant $x(x_f)$. The sub- and supercritical cases are separated by the dashed vertical lines. Data near the separating lines were discarded because in this range, higher-order terms are not negligible and Eq. (45) no longer describes the actual dynamics accurately. (a) $G_K = 1.0$, $x_f = 0.253$ and 0.358 for the sub- and supercritical sides, respectively. (b) $G_{si} = 0.2$, $x_f = 0.371$ for the subcritical side, and $G_{si} = 0.3$, $x_f = 0.358$ for the supercritical side. (c) $G_{si} = 0.13$, $G_{\rm K} = 0.282$, and $\beta = 0.75$, $x_{\rm f} = 0.163$ (subcritical) and 0.133 (supercritical). (d) $G_{si} = 0.13$, $G_{K} = 0.282,$ $\alpha = 0.13$, $x_f = 0.261$ (subcritical) 0.142 (supercritical).

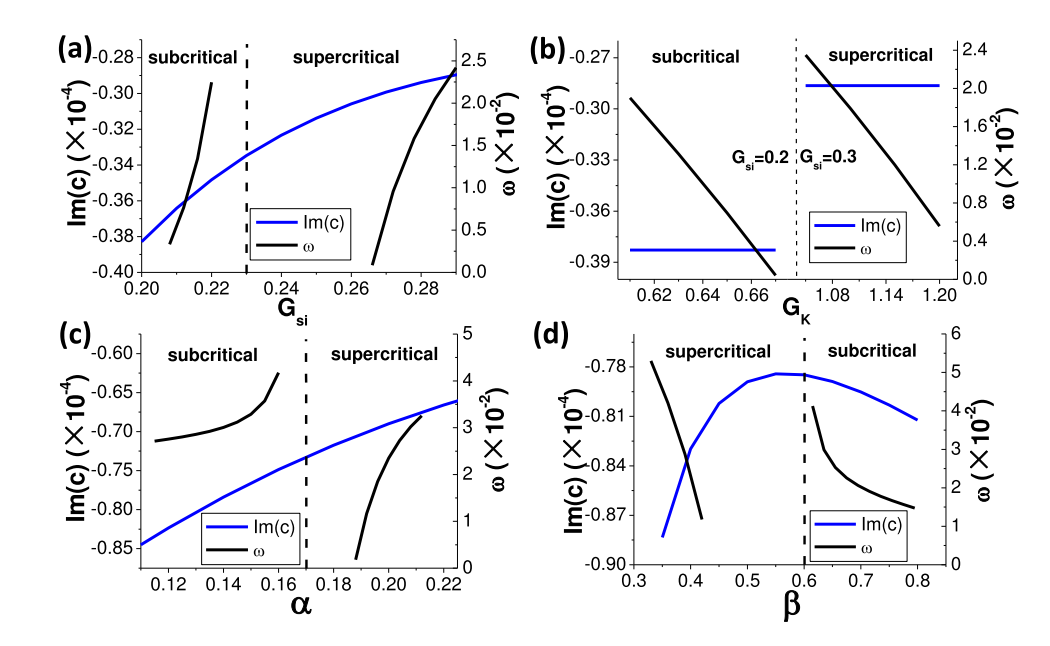


FIG. 7. Parametric modulation of the EAD frequency. The parameter set for each panel is identical to the corresponding one in Fig. 6. The data near the lines separating the sub- and supercritical cases are discarded. (a) Effect of G_{Si} . (b) Effect of G_K . (c) Effect of α . (d) Effect of β .

Next, we consider the inter-EAD period. Equation (46) gives the period around the bifurcation point $(T=2\pi/\omega)$. A^2 has already been obtained, and ω_0 can be calculated from Eq. (S29) in the supplementary material. Figure 7 shows the variations of $\mathrm{Im}(c)$ and the resulting ω for the parameter values. Actually, ω_0 varies little. In the present model, $\mathrm{Im}(c)$ remains negative with a low rate of variation. Therefore, A determines ω . From Eq. (46), we can see that any parameter variation that leads to an increase of A would reduce ω , while a reduction of A would have the opposite effect. An increase of G_{si} or α would reduce A so that they shrink the inter-EAD period. In contrast, an increase of G_K or β prolongs it. These findings confirm the results of our previous work, 19 in which qualitatively identical phenomena were generally found for several ventricular myocyte models. Thus, the normal form explains these phenomena.

V. LIMITATIONS

The main limitation of the present study lies in the model used. The LR1 model belongs to the first generation of models, which do not consider the intracellular Na⁺, K⁺, and Ca²⁺ cycling dynamics. This deficiency will be solved by the second- and third-generation models. The reason for using LR1 in the present study is that it is relatively simple and thus, suitable for analytical study, and it can still reveal some fundamental and general properties of cardiac myocytes. For example, Eq. (30) (which implies that an simultaneous increase of both LCC and KC currents can cause EAD) is consistent with the isoproterenol physiological study.²⁹ The EAD parametric ranges used for Fig. 3 are qualitatively similar to that of some other second-generation models (Figs. 10-14 in Appendix C). Finally, Figs. 6 and 7 confirm and explain our previous numerical results on the amplitude and period modulations in various models. 19 Hence, the results from the LR1 model are a good starting point and may suggest some practical uses.

However, besides the transmembrane ionic currents, intracellular ionic cycling also affects the membrane voltage via coupling with the LCC, late Na⁺ channel, and sodium–calcium exchange protein. Furthermore, recently, it has been reported that intracellular Ca²⁺ cycling may show self-oscillation and trigger EAD.³³ The association between EAD and intracellular ionic dynamics is not clearly understood, despite some suggestive studies (e.g., Refs. 33–35). LR1 type models are incapable of studying such complex effects, so we must turn to the newly developed multi-scale models. The present method and conclusions may serve as a foundation for future studies.

VI. SUMMARY

In the present paper, we investigated the conditions for the genesis of some arrhythmogenic behaviors and their dynamical properties. We obtained two main results: (i) the analytically closed forms of the sufficient parametric conditions for all possible scenarios (shown in Table II) and (ii) the normal form of LR1 for the Hopf bifurcation. The following important insights were obtained from the theoretical analyses:

- (1) The effects of the conductances. (i) EAD genesis is not only due to the net inward current but also needs a large enough calcium current. The threshold LCC conductance is irrelevant to the KC conductance. (ii) Both G_{si} and G_{K} need to be large enough to give rise to EAD. Hence, the previous hypothesis that the reduced repolarized reservoir facilitates EAD is not true. (iii) A general condition for RF_s was derived: an increase of LCC or a decrease of the KC currents may facilitate this type of behavior.
- (2) The effects of the kinetics. (i) Large γ facilitates EAD while small γ facilitates RF_s. We estimated the threshold between these states. (ii) The kinetics of LCC has a significant effect on EAD genesis. An increase of α increases the risk of EAD, RF_p, and RF_s. An increase of β has the opposite effect.

- (3) The influence of perturbations. We found that a reduction of V and x before the plateau phase of an AP may induce EAD. Moreover, an increase of V or a decrease of x at small γ may lead to RF_s. These findings may indicate possibilities for clinical treatments for EAD.
- (4) The normal form of EAD for the LR1 model was derived. We found that G_{si} is the deterministic parameter in changing the bifurcation type. Both the maximum amplitude and the number of occurrences of EAD for the supercritical bifurcation are larger than for the subcritical bifurcation. Hence, EAD due to a supercritical bifurcation may have a higher risk of causing arrhythmias.
- (5) Using the normal form, we explained that an increase of G_{si} or α reduces the amplitude and period, whereas an increase of G_K or β has the opposite effect. These phenomena are associated with the variation of the bifurcation point x_{p^*} . Any parameter change increasing x_{p^*} will shrink the amplitude and period, whereas decreasing x_{p^*} will have the opposite effect.

The present theory could be used to interpret and modulate EAD behavior. It could be extended to more complicated EAD dynamics involving intracellular ionic cycling.

SUPPLEMENTARY MATERIAL

See the supplementary material for the detailed derivations of the normal form shown in Eq. (44).

ACKNOWLEDGMENTS

This work was supported by the Fundamental Research Funds for the Central Universities (Grant No. 2017MS112 to X.H.), the Australian Research Council Center for Integrative Brain Function (Grant No. CE140100007 to D.Y.), and an Australian Research Council Laureate Fellowship Grant (No. FL140100025 to D.Y.).

APPENDIX A: FINDING (x_{p^*}, V_{p^*})

We will first derive the dependence of the Hopf bifurcation point (x_{p^*}, V_{p^*}) on the ionic conductance parameters G_{si} , G_K , and

Around the p state, which is relevant to EAD, the nonlinear functions x_{∞} , d_{∞} , f_{∞} , X_i , $K_{1\infty}$, τ_d , and τ_f can be approximated as polynomials. Then, I_{OSS} of Eq. (3) can be approximated as

$$I_{QSS}(V,x) = G_{si}P_{si}(V) + G_{K}xP_{K}(V) + G_{K1}P_{K1}(V) + G_{b}P_{b}(V),$$
(A1)

where

$$P_{si}(V) = (0.027V + 1.155)(-0.033V - 0.309)(V - E_{si}),$$

$$P_{K}(V) = (-0.0035V + 0.17)(V - E_{K}),$$

$$P_{K1}(V) = (0.0032V^{2} + 0.117V + 1.127)(V - E_{K1}),$$

$$P_{b}(V) = (V - E_{b}).$$

Figure 8 compares the approximate and original formulations. First, for the original model, there is little difference between the versions with and without I_{Kp} , so I_{Kp} was neglected throughout the present work. A comparison between the approximate and original I_{OSS} is shown in Fig. 8(a). Note that we need only the fitness around

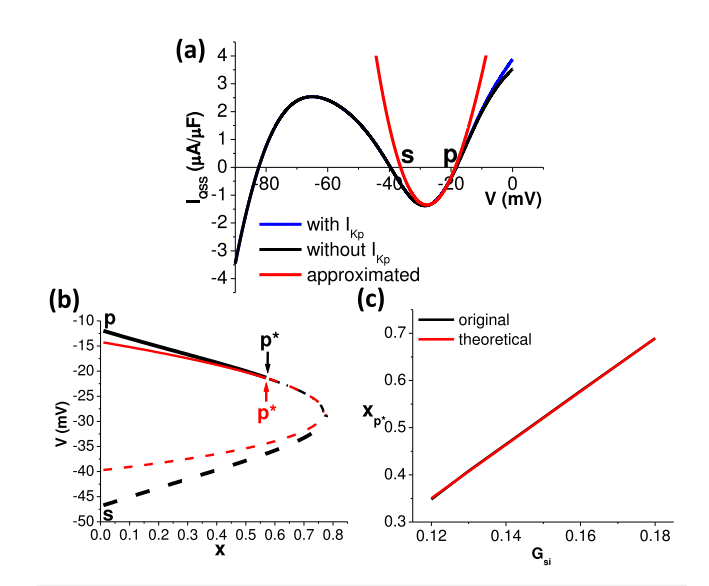


FIG. 8. Comparison between the original and approximate formulations. (a) Comparison of I_{QSS} . $G_{si}=0.16$, x=0.4. (b) Bifurcation diagram. $G_{si}=0.16$. The original and approximate bifurcation points p^* are denoted by black and red arrows, respectively. (c) Variation of approximate and practical x_{p*} as G_{si} is changed.

the p and s states that are associated with EAD. The bifurcation diagrams also coincide well [Fig. 8(b)]. Therefore, the approximate formulations reveal well the bifurcation of the original model.

By setting $I_{QSS} = 0$, we get from Eq. (A1),

$$x = -\frac{G_{si}P_{si}(V) + G_{K1}P_{K1}(V) + G_bP_b(V)}{G_KP_K(V)},$$
 (A2)

which can be substituted into Eq. (2) to get V_{p^*} at the Hopf bifurcation point p^* ,

$$V_{p^*} = Q(G_{si}, G_{K1}),$$

with all parameters except G_{si} , G_K , and G_{K1} being replaced by their control values. Note that G_K is naturally eliminated, and thus, V_{p^*} is independent of G_K . The function $Q(G_{si}, G_{K1})$ is continuous and smooth so that it can be expressed as a polynomial,

$$Q(G_{si}, G_{K1}) = \sum_{n=0}^{\infty} A_n(G_{K1}) G_{si}^n,$$
 (A3)

where $A_n(G_{K1})$ is a polynomial function of G_{K1} . We assume the terms with order higher than 2 can be ignored so that

$$V_{p^*} \approx A_2 G_{si}^2 + A_1 G_{si} + A_0. \tag{A4}$$

The rationality of this formulation was verified by the theoretical results.

The Lagrangian interpolation method²⁸ is applied to determine the coefficients A_n , as follows. First, we randomly choose three values of G_{si} within the physiologically reasonable range, say, $G_{si,i}$ (i = 1, 2, 3). Then, we fix $G_{K1} = G_{K1,1}$ and substitute $G_{si,i}$ into

Eq. (2) to obtain numerically three true $V_{p^*,i}$ values. Thus, V_{p^*} can be approximated as

$$\begin{split} V_{p^*} &= \frac{(G_{si} - G_{si,2})(G_{si} - G_{si,3})}{(G_{si,1} - G_{si,2})(G_{si,1} - G_{si,3})} V_{p^*,1} \\ &+ \frac{(G_{si} - G_{si,1})(G_{si} - G_{si,3})}{(G_{si,2} - G_{si,1})(G_{si,2} - G_{si,3})} V_{p^*,2} \\ &+ \frac{(G_{si} - G_{si,1})(G_{si} - G_{si,2})}{(G_{si,3} - G_{si,1})(G_{si,3} - G_{si,2})} V_{p^*,3} \\ &= A_{2,1} G_{si}^2 + A_{1,1} G_{si} + A_{0,1}. \end{split}$$

In this way, the values of $A_{n,1}$ (n=0,1,2), which depend on $G_{K1,1}$, can be determined. We repeat this process by fixing $G_{K1}=G_{K1,2}$ and $G_{K1,3}$ to get, correspondingly, $A_{n,2}$ and $A_{n,3}$. Finally, the coefficients A_n for n=0,1,2 can be determined by the Lagrangian interpolation as

$$\begin{split} A_n &= \frac{(G_{K1} - G_{K1,2})(G_{K1} - G_{K1,3})}{(G_{K1,1} - G_{K1,2})(G_{K1,1} - G_{K1,3})} A_{n,1} \\ &+ \frac{(G_{K1} - G_{K1,1})(G_{K1} - G_{K1,3})}{(G_{K1,2} - G_{K1,1})(G_{K1,2} - G_{K1,3})} A_{n,2} \\ &+ \frac{(G_{K1} - G_{K1,1})(G_{K1,2} - G_{K1,2})}{(G_{K1,3} - G_{K1,1})(G_{K1,3} - G_{K1,2})} A_{n,3} \\ &= r_{2,n} G_{K1}^2 + r_{1,n} G_{K1} + r_{0,n}, \end{split}$$

in which $r_{2,n}$, $r_{1,n}$, and $r_{0,n}$ are known numbers. Thus, the coefficients A_n for n = 0, 1, 2 can be explicitly expressed as

$$A_2(G_{K1}) = -147.51G_{K1}^2 + 424.43G_{K1} - 328.02,$$

$$A_1(G_{K1}) = 72.85G_{K1}^2 - 172.53G_{K1} + 125.02,$$

$$A_0(G_{K1}) = -7.03G_{K1}^2 + 19.13G_{K1} - 34.63.$$

We substitute Eq. (A4) into Eq. (A2) and assume that x_{p^*} can be approximated as a parabolic function of G_{si} . Then, by using Lagrangian interpolation again, x_{p^*} , can be obtained as

$$x_{p^*} \approx \frac{B_2 G_{si}^2 + B_1 G_{si} + B_0}{G_V},$$
 (A5)

with

$$B_2(G_{K1}) = -2.43G_{K1}^2 + 2.47G_{K1} - 0.71,$$

$$B_1(G_{K1}) = 0.45G_{K1}^2 - 0.46G_{K1} + 1.74,$$

$$B_0(G_{K1}) = 0.004G_{K1}^2 - 0.045G_{K1} - 0.07.$$

The agreement between the approximate and practical x_{p^*} on changing G_{si} was assessed, as shown by Fig. 8(c). The approximate result fits the original one perfectly.

An identical method was used for the kinetic parameters. The bifurcation point is expressed as

$$V_{p^*} = C_2 \beta^2 + C_1 \beta + C_0,$$

$$x_{p^*} = D_2 \beta^2 + D_1 \beta + D_0,$$
(A6)

with

$$C_2(\alpha) = \frac{-8.23}{\alpha^2} + \frac{2.83}{\alpha} - 0.67,$$

$$C_1(\alpha) = \frac{1.58}{\alpha^2} + \frac{20.81}{\alpha} - 2.19,$$

$$C_0(\alpha) = \frac{0.34}{\alpha^2} - \frac{2.97}{\alpha} - 33.3$$

and

$$D_2(\alpha) = \frac{0.84}{\alpha^2} - \frac{0.97}{\alpha} - 0.02,$$

$$D_1(\alpha) = \frac{-0.58}{\alpha^2} - \frac{0.46}{\alpha} + 1,$$

$$D_0(\alpha) = \frac{-0.01}{\alpha^2} + \frac{0.62}{\alpha}.$$

APPENDIX B: DETERMINING ΔV , Δx , δd , AND δf .

To obtain the theoretical curves in Fig. 3, the adjustable parameters ΔV , Δx , δd , and δf must be chosen carefully. As long as they satisfy certain conditions, the quality of the theoretical results are robust against the variability of their values. The conditions are as follows.

First, for EAD (i.e., scenario 1), $\Delta x > 0$ and $\Delta V < 0$ must be satisfied, because the orbit approaches p^* from upper left to lower right in the x vs V plane, whereas for RF_s (scenario 3), $\Delta x < 0$ and $\Delta V < 0$ must be satisfied because the orbit approaches s^* from upper right to lower left.

Second, consider δd and δf , which are associated with the quality of I_{D^*} and I_{S^*} . For I_{D^*} , we have

$$\begin{split} I_{p^*} &= -a\delta V - b\delta d - c\delta f \\ &\approx -b\delta d - c\delta f \\ &= -G_{si} f_{\infty} (V_{p^*} - E_{si}) \delta d - G_{si} d_{\infty} (V_{p^*} - E_{si}) \delta f \\ &= -G_{si} (V_{p^*} - E_{si}) \left(f_{\infty} \delta d + d_{\infty} \delta f \right) < 0, \end{split} \tag{B1}$$

$$\frac{dI_{p^*}}{dG_{si}} = -\left(V_{p^*} - E_{si} + G_{si}\frac{dV_{p^*}}{dG_{si}}\right)(f_{\infty}\delta d + d_{\infty}\delta f)
- G_{si}\frac{dV_{p^*}}{dG_{ci}}(V_{p^*} - E_{si})\left(\frac{df_{\infty}}{dV_{o^*}}\delta d + \frac{dd_{\infty}}{dV_{o^*}}\delta f\right) < 0, \quad (B2)$$

$$\begin{split} \frac{dI_{p^*}}{d\beta} &= -G_{si} \frac{dV_{p^*}}{d\beta} (V_{p^*} - E_{si}) \left(\frac{df_{\infty}}{dV_{p^*}} \delta d + \frac{dd_{\infty}}{dV_{p^*}} \delta f \right) \\ &- G_{si} \frac{dV_{p^*}}{d\beta} (f_{\infty} \delta d + d_{\infty} \delta f) > 0, \end{split} \tag{B3}$$

$$\frac{dI_{p^*}}{d\alpha} = -G_{si} \frac{dV_{p^*}}{d\alpha} (V_{p^*} - E_{si}) \left(\frac{df_{\infty}}{dV_{p^*}} \delta d + \frac{dd_{\infty}}{dV_{p^*}} \delta f \right)
-G_{si} \frac{dV_{p^*}}{d\alpha} (f_{\infty} \delta d + d_{\infty} \delta f) < 0.$$
(B4)

Note that the first term $a\delta V$ in I_{p^*} is much smaller than the other two terms, so that it can be ignored, meaning δV has little effect on

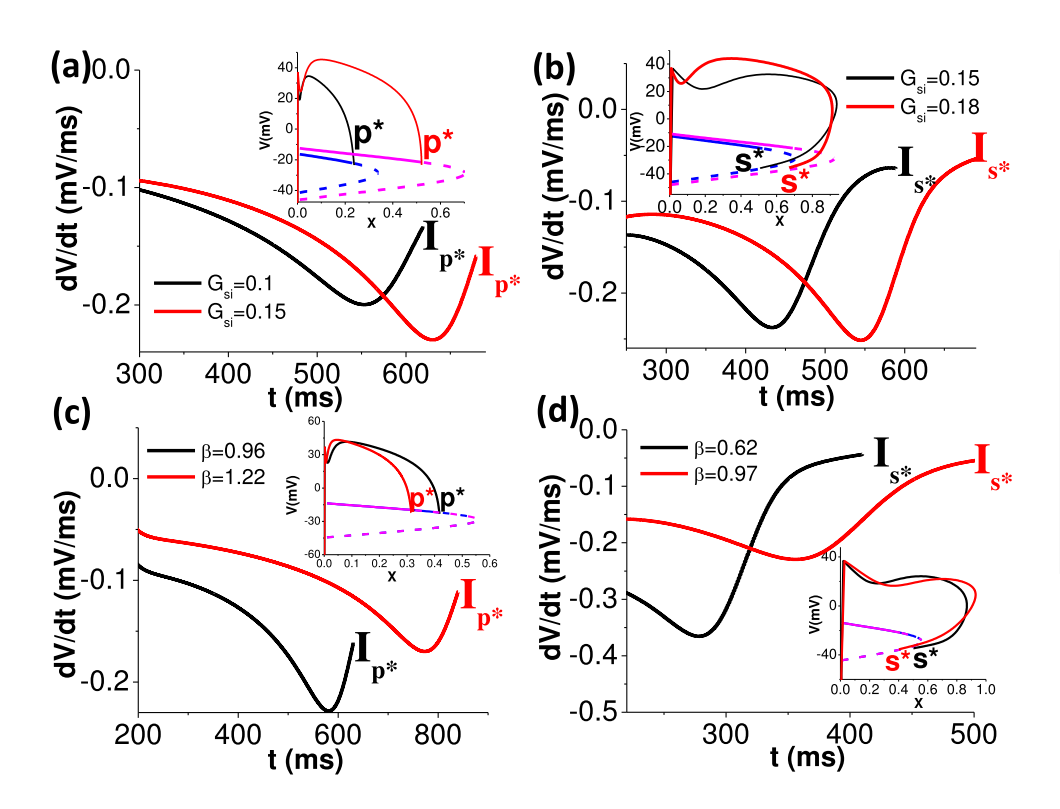


FIG. 9. Variation of I_{p^*} and I_{s^*} as the parameters are changed. The values at the end of the curves are roughly I_{p^*} and I_{s^*} . The inset in each panel shows the APs, which reach the critical points. The blue and magenta curves are the null-clines under different parameters. Note that the kinetics do not affect the null-cline. Different values of γ are used to finely chose the APs, for the black and red traces, respectively. (a) 5.72 and 2.41. (b) 0.181 and 0.467. (c) 3 and 6.32. (d) 0.149 and 0.1

the results. Thus, we fix it to -0.2 mV throughout this work. If we replace subscript p^* with s^* , then we have

$$I_{s^*} < 0, \quad \frac{dI_{s^*}}{dG_{ci}} > 0, \quad \frac{dI_{s^*}}{dB} < 0, \quad \frac{dI_{s^*}}{d\alpha} > 0.$$
 (B5)

The reasons for the above inequalities are as follows. Consider $dV/dt = -I \approx I_{p^*}$ and $dV/dt \approx I_{s^*}$ around p^* and s^* , respectively. Since V is always repolarizing to reach p^* and s^* , then I_{p^*} and I_{s^*} must be both smaller than 0. Equations (B2)–(B5) are based on observations of the APs near the critical points p^* and s^* , as illustrated in Fig. 9. We finely choose a specific AP that can reach the critical point. When it is sufficiently close to the critical point, the rate of change of the voltage dV/dt can roughly reveal the current I_{p^*} (or I_{s^*}). Figure 9 shows dV/dt as the AP approaches the critical point for different parameters. We can see that as G_{si} increases, dV/dt falls near p^* [Fig. 9(a)], whereas near s^* , it slightly increases [Fig. 9(b)]. On the other hand, as β increases, dV/dt increases near p^* , whereas it slightly decreases near s^* .

The results for α do not need to be calculated. $dI_{p^*}/d\alpha$ $(dI_{s^*}/d\alpha)$ must have the opposite sign as $dI_{p^*}/d\beta$ $(dI_{s^*}/d\beta)$ because $dV_{p^*}/d\alpha$ $(dV_{s^*}/d\alpha)$ and $dV_{p^*}/d\beta$ $(dV_{s^*}/d\beta)$ have the opposite signs [in the expression for V_{p^*} , α is in the denominators, whereas β is in the numerators; see Eq. (A6)].

Therefore, the choices of δd and δf should simultaneously satisfy Eqs. (B1)–(B5). If δd and δf are chosen in this way, the theoretical results in Eqs. (11)–(18) can reveal qualitatively well the real conditions. Therefore, the present analytical forms are robust and physically reliable.

APPENDIX C: RELEVANT RESULTS FROM OTHER MODELS

We numerically investigated the AP dynamics in five other updated ventricular myocyte models: (1) LRd for the guinea pig (by Luo and Rudy³⁶), (2) H_{UCLA} for the rabbit (by Huang *et al.*⁸), (3)

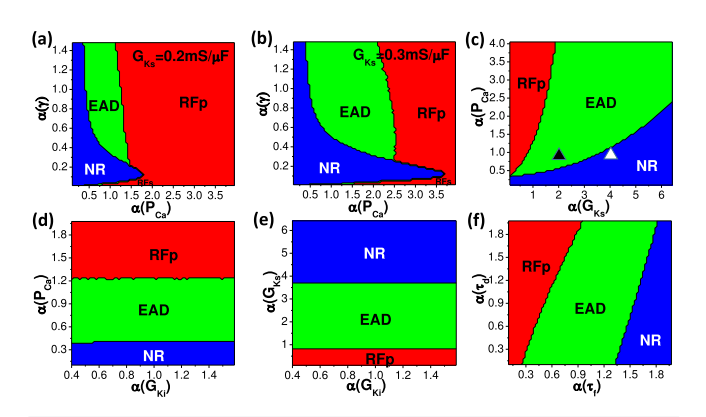


FIG. 10. LRd model. The control values are $P_{\text{Ca}} = 0.002 \, \text{cm/s}$ (permeability of membrane to Ca^{2+} , the modulation of which is equivalent to that of LCC conductance), $G_{\text{Ks}} = 0.2 \, \text{mS/}\mu\text{F}$ (KC conductance), $G_{\text{Ki}} = 0.75 \, \text{mS/}\mu\text{F}$ (conductance of the K1 channel), and $\gamma = 1$. Each coordinate indicates the fold change of the corresponding control value. (a) and (b) P_{Ca} vs γ . $G_{\text{Ks}} = 0.2 \, \text{mS/}\mu\text{F}$ and $G_{\text{Ks}} = 0.3 \, \text{mS/}\mu\text{F}$, respectively. (c) G_{Ks} vs P_{Ca} . The triangles indicate the parameter sets for plotting typical APs (black for EAD and white for NR), which are shown in Fig. 15. (d) G_{Ki} vs P_{Ca} . (e) G_{Ki} vs G_{Ks} . (f) τ_f vs τ_d .

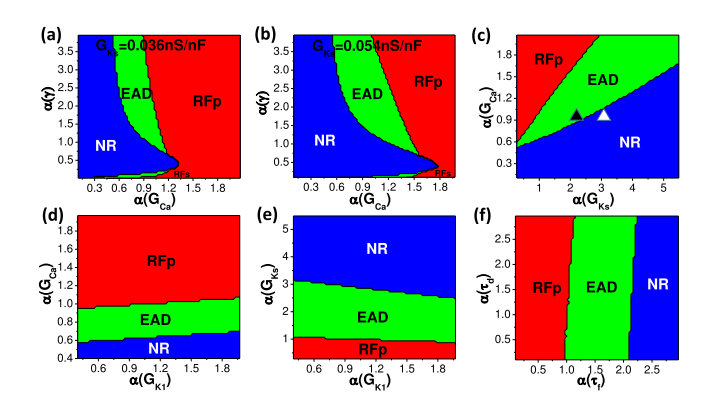


FIG. 11. TP04 model. The control values are $G_{\text{Ca}}=0.0008\,\text{cm}^3/(\mu\text{F}\,\text{s})$ (LCC conductance), $G_{\text{Ks}}=0.036\,\text{nS/pF}$, $G_{\text{K1}}=5.405\,\text{nS/pF}$ (conductance of the K1 channel), and $\gamma=2$. (a) and (b) G_{Ca} vs γ . $G_{\text{Ks}}=0.036\,\text{nS/pF}$ and $G_{\text{Ks}}=0.054\,\text{nS/pF}$, respectively. (c) G_{Ks} vs G_{Ca} . (d) G_{K1} vs G_{Ca} . (e) G_{K1} vs G_{Ks} . (f) τ_f vs τ_g .

TP04 for humans (by ten Tusscher *et al.*³⁷), (4) ORd for humans (by O'Hara *et al.*³⁸), and (5) GB for humans (by Grandi *et al.*³⁹). Figures 10–14 illustrate the parametric conditions for the behavior of the models. In all the figures, each coordinate is the fold change of the corresponding control value. As specific parameters are scanned, the others are fixed to their control values, as stated in the captions. For each model, we plot typical APs for NR and EAD (Fig. 15).

Although these models have different formulations and take into account intracellular ionic cycling, which is not modeled in LR1, the parametric conditions are similar to those of LR1 (with a few differences). Panels (a) and (b) in each figure are produced by different G_{Ks} values. We can see that the lowest LCC conductance for EAD genesis is nearly unchanged as G_{Ks} varies, which was noted in Sec. III C 1. In all the models, we can observe RF_s at small γ .

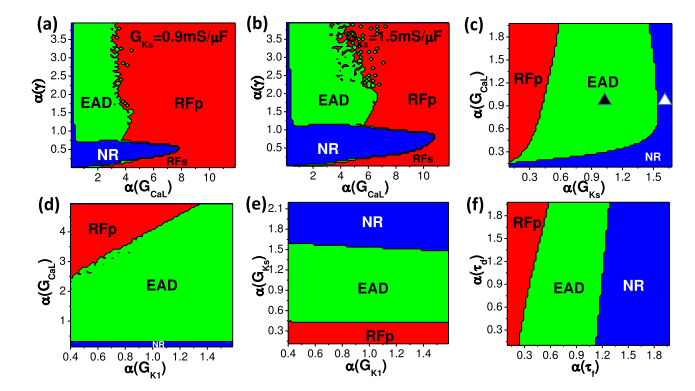


FIG. 12. H_{UCLA} model. The control values are $G_{CaL}=300\,\mathrm{mmol/(cm,C)}$ (LCC conductance), $G_{Ks}=0.9\,\mathrm{mS}/\mu\mathrm{F}$, $G_{K1}=0.3\,\mathrm{mS}/\mu\mathrm{F}$, and $\gamma=1$. (a) and (b) G_{CaL} vs γ . $G_{Ks}=0.9\,\mathrm{mS}/\mu\mathrm{F}$ and $G_{Ks}=1.5\,\mathrm{mS}/\mu\mathrm{F}$, respectively. (c) G_{Ks} vs G_{CaL} . (d) G_{K1} vs G_{CaL} . (e) G_{K1} vs G_{CaL} . (e) G_{K1} vs G_{K2} . (f) G_{K3} vs G_{K3} .

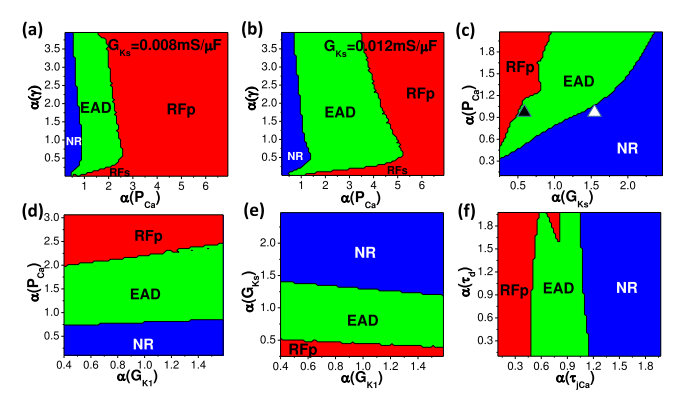


FIG. 13. ORd model. The control values are $P_{\text{Ca}} = 0.0003 \, \text{cm/s}$, $G_{\text{Ks}} = 0.008 \, \text{mS}/\mu\text{F}$, $G_{\text{K1}} = 0.1908 \, \text{mS}/\mu\text{F}$, and $\gamma = 1$. (a) and (b) P_{Ca} vs γ . $G_{\text{Ks}} = 0.008 \, \text{mS}/\mu\text{F}$ and $G_{\text{Ks}} = 0.012 \, \text{mS}/\mu\text{F}$, respectively. (c) G_{Ks} vs P_{Ca} . (d) G_{K1} vs P_{Ca} . (e) G_{K1} vs G_{Ks} . (f) τ_{JCa} vs τ_d . In this model, τ_{JCa} has the major role in modulating the LCC kinetics.

However, also note that these models have some differences with the LR1 model. The first is the RF $_p$ boundary in panels (a) and (b). In LR1, this is a straight line, whereas in the other models, it is curved. We think that this should be attributed to the stability of the q state. In LR1, it is always globally stable. However, in the other models, its stability depends on more complex factors, e.g., the intracellular calcium cycling. Second, RF $_s$ differs a little in the ORd and GB models. In the RF $_s$ region, as γ becomes larger, EAD occurs rather than NR. We hypothesize that in these models, the saddle is a saddle focus in the high-dimensional phase space so that the orbit rotates around the saddle as it leaves the point via the unstable manifold, showing EAD-like voltage oscillations. We expect that all the differences are due to the complicated intracellular ionic dynamics, which needs further investigation.

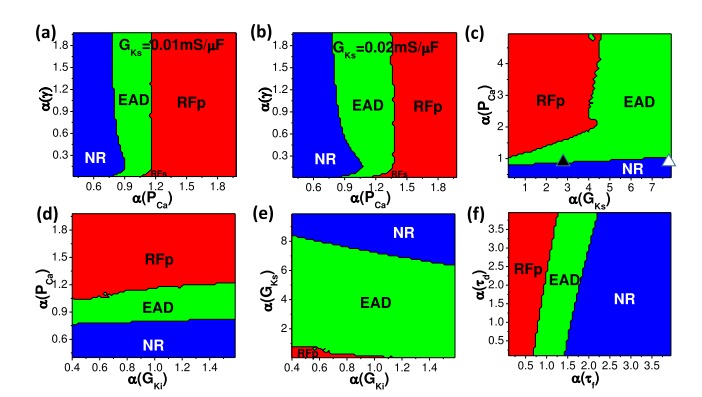


FIG. 14. GB model. The control values are $P_{\text{Ca}} = 0.0001725 \, \text{cm/s}$, $G_{\text{Ks}} = 0.01 \, \text{mS}/\mu\text{F}$, $G_{\text{Ki}} = 0.195 \, \text{mS}/\mu\text{F}$, and $\gamma = 1$. (a) and (b) P_{Ca} vs γ . $G_{\text{Ks}} = 0.01 \, \text{mS}/\mu\text{F}$ and $G_{\text{Ks}} = 0.02 \, \text{mS}/\mu\text{F}$, respectively. (c) G_{Ks} vs P_{Ca} . (d) G_{Ki} vs P_{Ca} . (e) G_{Ki} vs G_{Ks} . (f) τ_{f} vs τ_{d} .

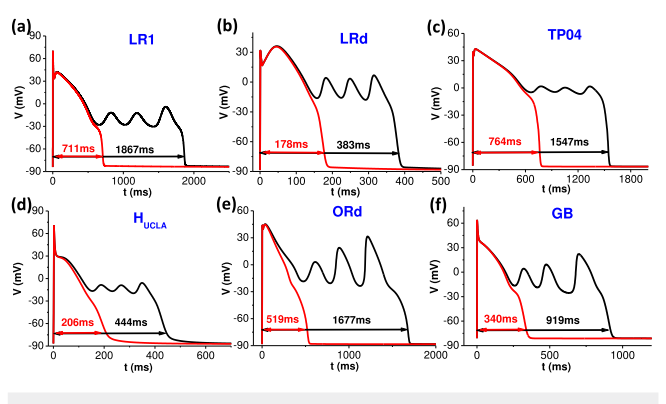


FIG. 15. Typical APs of the models. The parameters are set to the control values except G_{Ks} , which was varied so that EAD transitioned to NR. We plot APs with three EADs to compare the typical EAD time scales of the different models. The APDs are indicated on the panels. The $\alpha(G_{Ks})$ values are (the first number is for EAD and the second is for NR) (a) 0.92, 1.06; (b) 2, 4; (c) 2.2, 3; (d) 1.1, 1.6; (e) 0.56, 1.5; and (f) 2.8, 7.8. These parameter sets are indicated by triangles in the corresponding G_{Ks} vs G_{Cal} planes of Fig. 3(b) and Figs. 10-14.

REFERENCES

- ¹P. F. Cranefield, Circ. Res. 41, 415 (1977).
- ²G. Yan, Y. Wu, T. Liu, J. Wang, R. A. Marinchak, and P. R. Kowey, Circulation 103, 2851 (2010).
- ³M. R. Rosen, Hellenic J. Cardiol. **50**(3), 170 (2009).
- ⁴C. January, V. Chau, and J. Makielski, Eur. Heart J. 12(Suppl. F), 4 (1991).
- ⁵D. Sato, L.-H. Xie, A. A. Sovari, D. X. Tran, N. Morita, F. Xie, H. Karagueuzian, A. Garfinkel, J. N. Weiss, and Z. Qu, Proc. Natl. Acad. Sci. U.S.A. 106, 2983
- ⁶Y. Xie, D. Sato, A. Garfinkel, Z. Qu, and J. N. Weiss, Biophys. J. 99, 1408 (2010).
- ⁷M. Maruyama, S.-F. Lin, Y. Xie, S.-K. Chua, B. Joung, S. Han, T. Shinohara, M. J. Shen, Z. Qu, J. N. Weiss, and P.-S. Chen, Circ. Arrhythm. Electrophysiol. 4, 103
- (2011). $^{\bf 8}$ X. Huang, T. Y. Kim, G. Koren, B.-R. Choi, and Z. Qu, Am. J. Physiol. Heart Circ. Physiol. 311, H1470 (2016).
- ⁹W. Liu, T. Y. Kim, X. Huang, M. B. Liu, G. Koren, B.-R. Choi, and Z. Qu, J. Physiol. 596, 1341 (2018).
- ¹⁰M. Rosen, J. Moak, and B. Damiano, Ann. NY Acad. Sci. 427, 84 (1984).
- ¹¹D. Roden, Pace 21, 1029 (1998).

- ¹²Z. Qu, L.-H. Xie, R. Olcese, H. S. Karagueuzian, P.-S. Chen, A. Garfinkel, and J. N. Weiss, Cardiovasc. Res. 99, 6 (2013).
- 13 O. Koval, X. Guan, Y. Wu, M. Joiner, Z. Gao, and B. Chen et al., Proc. Natl. Acad. Sci. U.S.A. 107, 4996 (2010).
- ¹⁴M. Yamada, K. Ohta, A. Niwa, N. Tsujino, T. Nakada, and M. Hirose, J. Membr. Biol. 222, 151 (2008).
- 15 D. X. Tran, D. Sato, A. Yochelis, J. N. Weiss, A. Garfinkel, and Z. Qu, Phys. Rev. Lett. 102, 258103 (2009).
- ¹⁶C. Luo and Y. Rudy, Circ. Res. **68**, 1501 (1991).
- 17 M. Chang, C. Chang, E. de Lange, L. Xu, B. O'Rourke, H. Karagueuzian, L. Tung, E. Marban, A. Garfinkel, J. Weiss, Z. Qu, and M. Abraham, Biophys. J. **102**, 2706 (2012).
- ¹⁸P. Kügler, PLoS ONE **11**, e0151178 (2016).
- ¹⁹X. Huang, Z. Song, and Z. Qu, PLoS Compt. Biol. **14**, e1006382 (2018).
- ²⁰M. C. Cross and P. C. Honhenberg, Rev. Mod. Phys. 65, 851 (1993).
- ²¹Y. A. Kuznetsov, Elements of Applied Bifurcation Theory, 3rd ed. (Springer, 2004).
- ²²S. Guo and J. Wu, Bifurcation Theory of Functional Differential Equations (Springer, New York, 2013).

 ²³ M. C. Cross, Phys. Fluids **23**, 1727 (1980).
- ²⁴D. Yang and P. A. Robinson, *Phys. Rev. E.* **95**, 042410 (2017).
- ²⁵B. Echebarria and A. Karma, Phys. Rev. E. **76**, 051911 (2007).
- ²⁶J. P. Keener and J. Sneyd, Mathematical Physiology (Springer, New York, 1998).
- ²⁷S. Rush and H. Larsen, IEEE Trans. Biomed. Eng. 25, 389 (1978).
- ²⁸W. H. Press, S. A. Teukolsky, W. T. Vetterling, and B. P. Flannery, *Numeri*cal Recipes in Fortran 77: The Art of Scientific Computing, 2nd ed. (Cambridge University Press, 1992).
- ²⁹G. Liu, B.-R. Choi, O. Ziv, W. Li, E. de Lange, Z. Qu, and G. Koren, J. Physiol. 590, 1171 (2012).
- 30 Y. Xie, E. Grandi, J. L. Puglisi, D. Sato, and D. M. Bers, J. Mol. Cell. Cardiol. 58, 153 (2013).
- 31 C. Antzelevitch, Eur. Heart J. 3(Suppl. K), K2 (2001).
- ³²Z. Qu and D. Chung, PLoS ONE 7(8), e43587 (2012).
- ³³D. Wilson, B. Ermentrout, J. Němec, and G. Salama, Chaos 27, 093940
- ³⁴Z. Song, C. Y. Ko, M. Nivala, J. N. Weiss, and Z. Qu, Biophys. J. **108**, 1908 (2015).
- 35 Y. Kurata, K. Tsumoto, K. Hayashi, I. Hisatome, Y. Kuda, and M. Tanida, Front. Physiol. 10, 1545 (2020).
- ³⁶C.-H. Luo and Y. Rudy, Cir. Res. 74, 1071 (1994).
- ³⁷K. H. W. J. ten Tusscher, D. Noble, P. J. Noble, and A. V. Panfilov, Am. J. Physiol. 286(4), H1573 (2004).
- ³⁸T. O'Hara, L. Virág, A. Varró, and Y. Rudy, PLoS Comput. Biol. 7(5), e1002061
- ³⁹E. Grandi, F. S. Pasqualini, and D. M. Bers, J. Mol. Cell. Cardiol. 48, 112 (2010).